DOI: 10.12442/j.issn.1002-185X.20240798

Study on microstructure and properties of the Mg/Fe dissimilar metal joint via magnetic pulse welding

Xie Jilin[1], Li Shimeng[2], Wang Yaping[3], Liu Dongya[4], Liu Xiaofang[5], Chen Yuhua[6]

Abstract: In the paper, AZ31B magnesium alloy/DC56D steel dissimilar metal incompatible metals are welded using magnetic pulse welding. We have comparatively studied the effect of Primary and Secondary welding on the welded interface. Macroscopic morphology, microstructure, and interfacial structure have been analyzed using techniques such as scanning electron microscopy (SEM), energy dispersive spectroscopy (EDS), and X-ray diffraction (XRD). The results show that magnetic pulse welding of Mg/Fe dissimilar incompatible metals is realized using Al interlayer as a bridge of deformation and diffusion. The studies display that the AZ31B/Al1060 interface appears the typically wavy interface, a transition zone exists in the joint interface and may cause extremely complex microstructure. The transition zone structure differs from AZ31B Magnesium and 1060 Al alloys, which could be brittle intermetallic compounds of Al_3Mg_2 and $Al_{12}Mg_{17}$. The transition zone is mainly on the Al side, with a maximum thickness of about 13.53μm in the Al transition layer. We observed incomplete melting layers of varying thicknesses at the Primary weld interface and micron-sized hole defects in the transition zone of the Secondary weld interface. Al1060/DC56D interlayer is mainly straight in shape, with only a small number of transition zones in the joint interface distributed intermittently across the interface, and the transition zone is characterized by the presence of FeAl3 brittle intermetallic compounds, with a maximum thickness of about 2.43 μm.

Keywords: Magnetic Pulse Welding; mechanical properties; microstructure; fracture morphology; Primary and Secondary weld

Steel is a structural material with high strength, excellent plasticity, and good weldability, which is the broadest applicable material in motor vehicles, accounting for 55% of total vehicle weight[1]. Mg is one of the lightest structural metal materials and its density is 1.74 g/cm^3, giving it a superiority that sets it apart from other materials[2]. Mg alloy has high specific strength, high specific stiffness, low density, high damping, electromagnetic shielding, good dimensional stability, thermal conductivity, and electrical conductivity, as well as excellent casting, cutting, processing performance, and easy recycling, etc., known as the "21st Century Green Engineering Materials"[3]. Therefore, welding Mg alloy into steel increases the application value of magnesium alloy and facilitates the development of automotive lightweight technology.

Dissimilar metal joints meet the material requirements for different working conditions and leverage each other's performance advantages. Due to the crystal structure of Mg being hexagonal close-packed(HCP) at environmental temp and Fe being body-centered cubic(BCC), the structure leads to smaller solid solubility between the two(<0.00041%). Mg and Fe are likely to form intermetallic compounds, their physical properties are vast differences including melting temperature, thermal conductivity, coefficient of thermal expansion (CTE), and lattice structure[4]. The challenge lies in joining magnesium alloys and steel. Generally, there are two ways to achieve metallurgical bonding for Mg/Fe, which have widely differing physical properties, including directly adding interlayer[5] and increasing other alloy elements in base metals[6]. Fe-Al intermetallic compounds(IMCs) replace Fe-Mg IMCs with poorer mechanical properties during friction stir welding of steel to magnesium alloys[7]. The addition of Zn coating between AZ31 and steel hinders Fe-Mg IMCs generation[8]. The strength of the weld is subjected to microstructure and thickness in the interlayer[9].

In addition, diffusion welding, fusion welding, resistance spot welding, and ultrasonic spot welding are also used for joining Mg/Fe, which invariably follow the above methods. For example, adding Cu[10,11] and Ni interlayers[12] enabled successful diffusion joining of Mg/Fe. Song, Li, and Zhao et al.[13–15] reduced IMCs in Mg/Fe laser welding using elemental modulation and adding Ni foil. Similarly, Mg/Fe resistance spot welding and ultrasonic spot welding experiments added Zn foil and Al-Si coating[16–18]. The above cases proved that adding interlayers contributes to improved interfacial mechanical properties. However, partial Mg/Fe solid phase welds, especially those involving the

interlayer field, are still unexplored.

In recent years, scholars have increasingly studied the application of high-speed impact welding in dissimilar alloys. Vaporative Foil Actuator Welding (VFAW)[19] is a solid-state impact joining process that fuses two boards by rapidly evaporating the foil. The resulting expanding gases propel the flyer toward the substrate at high speeds. Du et al.[20] successfully joined NiTi/Al-Mg alloys by the VFAW technique, the results indicate a correlation between interface morphology and welding parameters, and the joint performance increased and then decreased. Magnetic pulse welding(MPW)[21] is a solid-phase welding technology whose principles are to use electromagnetic force to make two materials collide at high speed and generate metallurgical bonding. The technology is defined by high efficiency, environment-friendly, simple operation, and easy-to-realize automation. It is unlikely to form a heat-affected zone(HAZ) due to its quick process, and less formation of IMCs in the joint[22]. So, Magnetic pulse welding is very suitable for joining dissimilar metals such as Al/Mg[23–25]. Likewise, Wang et al[26]. explored the formation principle of the Al/Cu interface, Li et al.[27] used numerical simulation to reveal the mechanism of the interfacial wave formation, and Sapanathan et al.[28] carried out a study of the pore nuclear and growth process. In addition, MPW is also widely used in Al/Fe welding[29], for example, amorphization and recrystallization[30], fatigue fracture properties, the correlation between interface morphology and discharge energy, and the effect of Zn coatings on phase transitions during MPW of Al/Fe [31–33].

In the paper, AZ31B/Al1060/DC56D three-layer composite structure prepared by the MPW technique, using a characterization of Al compatible and react with Mg and Fe, which AZ31B magnesium alloy as fly plate, AA1060 as interlayer, DC56D as substrate plate. Mechanical properties of welded joints, fracture morphology, welding interfacial morphology, and microstructure are analyzed.

1 Experiment

1.1 Experimental equipment

Magnetic pulse welding equipment is an electromagnetic pulse welding system called XtraPulse 75/25. It has a maximum voltage of 25KV and a maximum discharge energy of 75KJ, manufactured by Chongqing Pulsa Technology Co. The equipment consists of a control system, an energy storage system, and a work table. The control system is the nerve center of the entire magnetic pulse welding equipment which is responsible for controlling the setting of the welding power source and the energy output mode. The energy storage system incorporates inductive-capacitive circuits and some impedance actuators. A large current flows through the coil creating a primary magnetic field when the capacitor is discharged. This field induces a powerful secondary current in the flyer. However, the secondary current in the flyer flows in the opposite direction to the coil current, resulting in a strong repulsive Lorentz force between them. This force allows the flyer to collide with the substrate at a very high speed. The coils utilized in this study have an E-shaped configuration.

1.2 Materials and Approaches

Bonding Mg alloy and steel conducted magnetic pulse welding using Al as interlayer. AZ31B Mg alloy and DC56D steel are utilized respectively by fly and substrate plate, with the former dimensions being 40×80×1 mm³ and the latter size being 40×80×0.7mm³. The middle layer is made of pure Al with dimensions of 40×20 ×0.2mm³, and the driver plate is also pure Al with dimensions of 40 x 80 x 1mm³. Its chemical composition is detailed in Table 1. The base material's surface was wiped with alcohol to ensure cleanliness before welding. Magnetic pulse welding was performed using the lap method, as depicted in Fig. 1(a). A high-temperature-resistant plastic spacer is applied to separate the flyer from the substrate to ensure a certain initial gap during the welding process. During welding, the coil under the action of the pulse current, generates an alternating magnetic field so that the fly plate will produce an induced current. When the induced current results in electromagnetic interaction with the coil magnet, it generates Lorentz force to drive the fly plate at a high-speed collision with the substrate plate to form a weld. The magnetic pulse welding principle is shown in Fig. 1(b). Two welding methods are used in this experiment: primary and secondary welding. Primary welding involves applying the Al interlayer directly on the Mg alloy fly plate, with the flyer together with the collision of the substrate to form a connection. Secondary welding begins with the use of a 1mm thick Al plate as the driver plate which a layer of insulation is applied to the driver board to prevent contact between the driver board and the intermediate layer. Followed by the drive plate connected to the Al middle layer and DC56D steel(substrate plate), ultimately, Mg alloy as a fly plate with its welding. Specific welding schematics for these two welding methods are shown in Fig.

1(c,d).

The welding parameters in this study were discharge energy of 26, 28, 30, and 32 KJ and a welding gap of 1.5 mm. Weld samples were obtained by both Primary and Secondary welding, and eight weld combinations were obtained and tested for their mechanical properties. Based on the mechanical properties of the welded samples, the two sets of parameters with the best overall performance were selected from the Primary and Secondary welded samples for subsequent microstructural characterization and analysis, respectively.

Table 1 Chemical composition of base metal (mass fraction)

Materials	Mg	Mn	Si	Fe	Ni	Al	Zn
AZ31B	Bal.	0.2	0.08	0.003	0.001	3.0	1.0
	Fe	C	S	Mn	P	Nb	Si
DC56D	Bal.	0.002	0.005	0.38	0.002	0.02	0.008
	Al	Cu	Si	Mg	Zn	Ti	Fe
A1060	Bal.	0.05	0.25	0.04	0.06	0.03	0.35

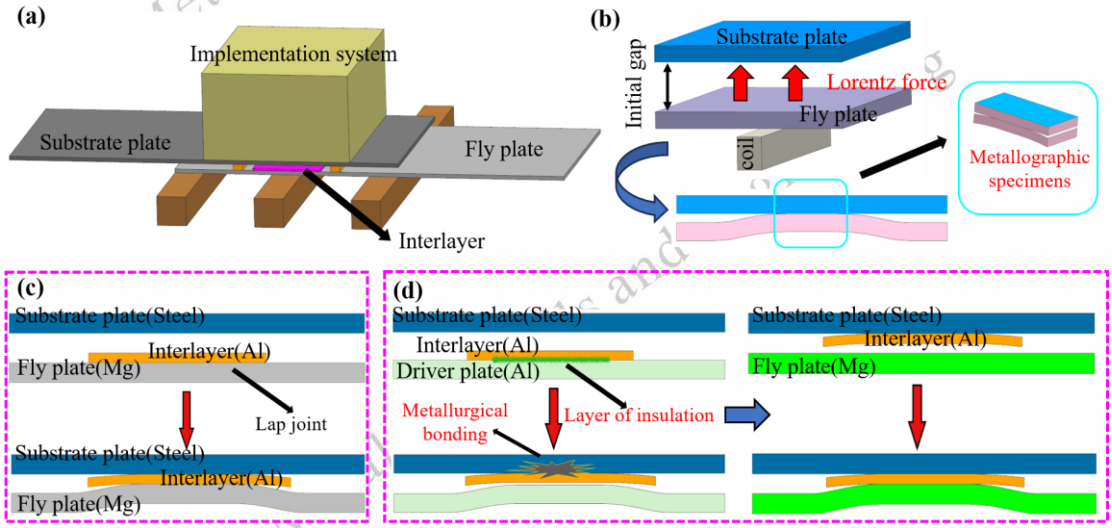

Fig.1 AZ31B/Al1060/DC56D Magnetic Pulse Welding Process and Principle Schematic: (a) Lap Method Schematic with Interlayer, (b) MPW Principle and Sampling Method, (c) Primary Welding Schematic(Fe, Al and Mg plate once weld), (d) Secondary Welding Schematic(First Al and Fe bonding, then Mg and Al bonding).

To study the microstructure in the bonded interface, the specimens perpendicular to the circumferential weld seam were cut using wire electrical discharge machining (WEDM). Rough grinding, fine grinding, and polishing treatments are executed with sandpaper after the cold mosaic of the specimen. A scanning electron microscope(SEM), model Phenom-XL-SED, and energy disperse spectroscopy(EDS), model Oxford INCAx-act, are implemented to analyze the interface morphology and microstructure of the welded joints. Instron 5540 precision tensile machine is employed for Tensile shear testing of the welded joint, and the tensile rate is 1.5 mm/min.

2 Results and Discussion

2.1 Macroscopic morphology of welded joints

The macroscopic morphology of the primary and secondary welded AZ31B/DC56D MPW specimens are shown in Fig.2. The total length of the welded zone is about 120mm, of which the range of overlap area is about 20×40 mm. The fly plate Mg alloy deformed region is located in the overlap area, and the most severe deformation in this region resembles an elliptical shape. The welded seam lies in the largest deformation area.

The width of the maximum deformation area (S) (mm) of AZ31B/DC56D MPW specimens under varying discharge energies and welding methods is presented in Table 2. It is noted that the various welding methods do not affect the width S, while the discharge energy does impact the width S. The width S increases with higher discharge energy, but the magnitude is small. Yuan et al.[34] showed that the width s is affected by the combination of discharge energy, initial gap, and coil width. When the initial

gap is kept constant, the flying plate receives more energy as the discharge energy increases, resulting in a larger deformed degree. However, due to the influence of coil width and initial clearance, the deformation does not rise infinitely with the enlargement in discharge energy; rather, it reaches a peak value.

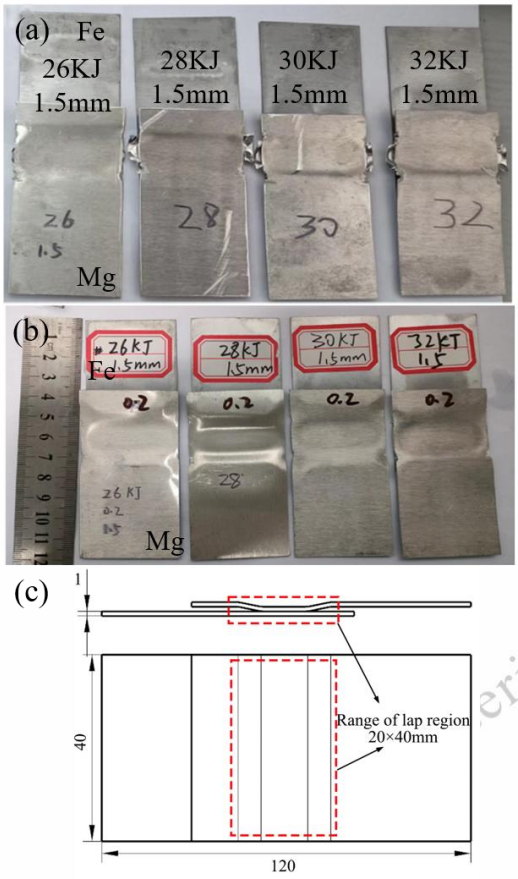

Fig.2 Macroscopic morphology of MPW specimens and its size: (a)primary weld, (b)secondary weld, (c)size specification of the tensile sample of the lap joint.

2.2 Effect of discharge energy on tensile properties

The investigation examined the mechanical properties of Mg/Fe joints affected by different discharge energies and welding techniques. The load-displacement curves of Mg/Fe joints for primary and secondary welding at varying energies are illustrated in Fig.3 (a) and (b), respectively. The two combined mechanical properties show a trend of increasing and then decreasing with the increase of discharge energy, as depicted in Fig. 3. When the discharge energy is 28 kJ, both welded joint loads reach their maximum, resulting in interface failure. However, as shown in Fig. 3, the performance of the welded joints from the secondary welding process appears to be superior. Further in-depth studies are conducted for the welded joints of secondary welding.

As the thickness of Al interlayer is only 0.2mm, the interlayer is basically detached on both sides of Mg and Fe after tensile fracture. To better analyze the fracture macroscopic morphology, the cleaner and more obvious samples in the secondary welding were selected for observation. Tensile-shear test and failure patterns in the welded joint of secondary welding are shown in Fig.3(c), in which the failure patterns at the joint only have welded zone failures(interfacial failures on the Mg side). The actual photographs of the Mg alloy failed welded joints are shown in Figure 3(c). The fracture shows an elliptical weld as a valid weld, and the weld channel's width is about 1 mm. It is possible to form a jet on the surface of the weld metal only at the right speed and collision angle so that occurrence of a good metallurgical bonding of the weld metal. There is enough collision velocity and the collision angle is small in the welding central region which makes the metal surface unable to form a jet, so the formation of an annular welding seam[35].

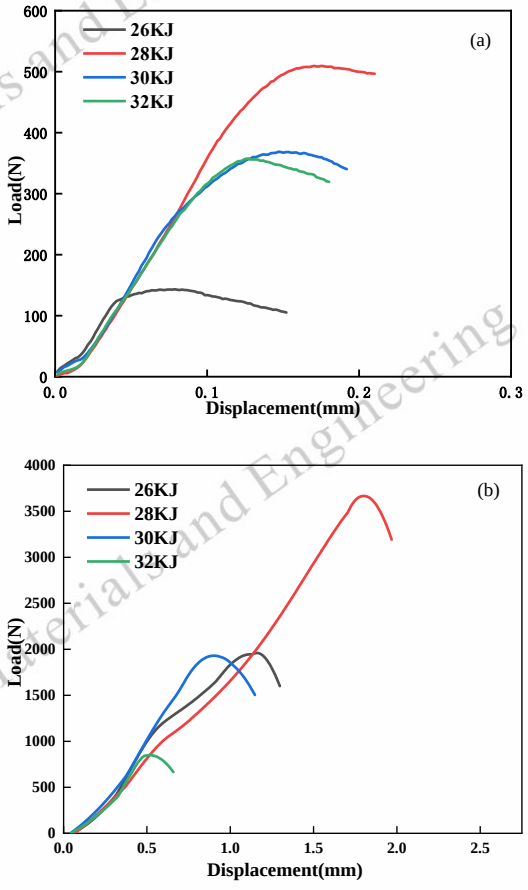

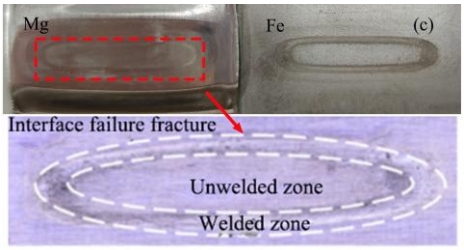

Fig.3 Load-displacement curves of Mg/Fe weldments: (a) primary weld, (b) secondary weld, (c)Fracture macroscopic morphology.

We analyzed the microstructural evolution of the Primary weld and Secondary weld using SEM under different process parameters better to understand the reasons for the variation in weld quality. These parameters included energy levels of 28KJ and 32KJ, as well as a 1.5mm gap. Figure 4 shows a cross-section of a Mg/Fe MPW welded joint with an Al intermediate layer, as observed by SEM. Fig. 4(a)(b) displays the interface morphology of the Primary weld. In Fig. 4(a), the Mg/Al interface and the Al/Fe interface are straight, while the Al side of the Al/Fe interface shows an incomplete fusion zone, which includes unmelted lamps Al and Fe, and a melted mixed structure. In Fig. 4(b), there are bulks of unfused structure at the Mg/Al interface and the Al/Fe interface appears wavy shapes, while not as obvious as in Fig. 4a. The metal jet spatter solidifies at the interface and the subsequent MPW process is insufficient to remelt it so that unmelted metal particles appear at the interface. Similarly, the Al/Ti MPW process has incompletely melted particles, reducing the mechanical properties of the joints[36]. Fig. 4(c)(d) displays the interface morphology of the Secondary weld, in which it is apparent that there are two welds on both sides of the interlayer. The interfaces between the Mg alloy and the Al interlayer, as well as between the Al interlayer and the steel, exhibit wavy patterns. It is evident that there is still a flat interface at the Al/Fe boundary, and the magnitude of the wave interface is minimal. Based on the above observations, the welding energy in the Primary weld is randomly distributed between the two interfaces resulting in poor interfacial bonding, so that the interfacial waveform changes and the amount of unmelted structure decreases with the welding energy increases. In contrast, Secondary welding does not suffer from the energy distribution problem during the single welding process. Faes et al.[37] found steel fragments after plastic deformation at the interface of magnetic pulsed welded copper and steel tubes, which was attributed to insufficient elemental diffusion mixing. This is also confirmed by the study of Patra et al[38].

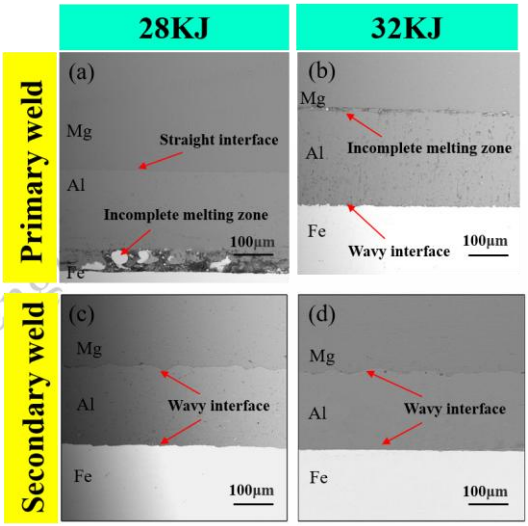

Fig.4 SEM image of Mg/Al/Fe bonding interface: (a)(c) 28 KJ-Primary and second weld, (b)(s) 32 KJ-Primary and second weld.

To observe the evolution of the welded interface in detail, we observed the welded interface using scanning electron microscopy (SEM) and energy dispersive spectroscopy (EDS) at high magnification, respectively. Figure 5 shows the typical morphology of the Primary weld, where (a-d) and (e-h) are the microscopic morphology of the Mg/Al and Fe/Al interfaces, respectively. By comparing the interfaces at different welding energies, it is found that the welded interface changes from straight to wavy with the increase of welding energy, accompanied by the rise of the thickness of the transition layer. The Al/Fe interface of the 28KJ sample was wrinkled to varying degrees, while no similar phenomenon was found in the 32KJ sample. This results from plastic deformation of the interface due to insufficient welding energy. In addition, the morphology and the thickness of the transition layer at the Mg/Al and Fe/Al interfaces are not consistent, which is caused by the difference in the physical properties of the materials. The EDS line scan results of the corresponding areas in the figure also show that the increase in welding energy leads to a wider range of elemental diffusion, which is more obvious in the Mg/Al interface; a clear elemental 'platform phase' can be found in the line scan in Fig. 5II, which may lead to the generation of new phases in this area. Points (1-4) in the SEM figure are labeled as the positions of the EDS point scans, and the corresponding results of the analyses are presented in Table. 3. It can be found that more IMCs are generated at the Mg/Al interface from Table. 3, which is the main reason why the mechanical properties of the Primary weld samples at 32 KJ welding energy are lower than those of

the corresponding 28KJ.

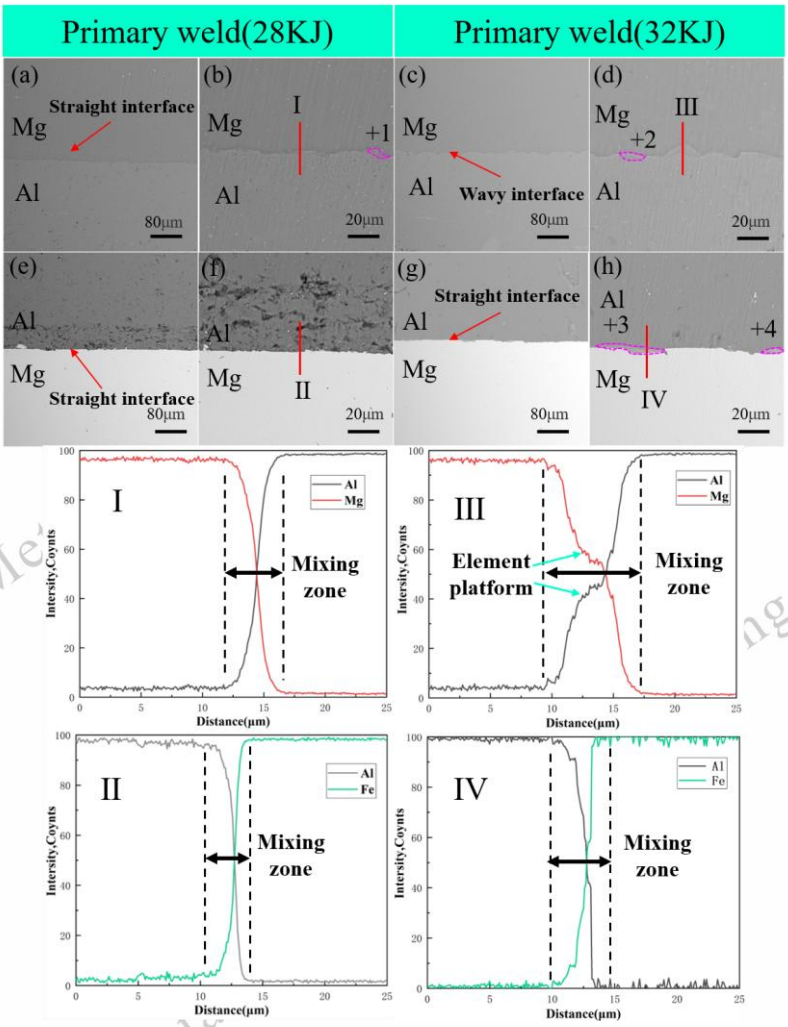

Fig.5 SEM images and EDS line scans of the Mg/Al/Fe bonded interface at different discharge energies(Primary weld): (a) (b) (e) (f) 28 KJ, (c) (d) (g) (h) 32 KJ, (a-d) for the Mg/Al side interface, (e-h) for the Al/Fe side interface.

Table. 3 EDS results for points in Figure 5(atomic fraction,%)

Position	Mg	Al	Fe	Possible phase
1	55.06	44.94		Al_3Mg_2+$Al_{12}Mg_{17}$
2	60.57	39.43		$Al_{12}Mg_{17}$
3		90.26	9.74	Solid solution of Al
4		73.70	26.30	$FeAl_3$+Al

Figure. 6 illustrates a typical regional SEM micrograph of the two connected interfaces of the Secondary weld. Figures 6(a-d) and (e-h) show the microscopic morphology of the Mg/Al and Al/Fe interfaces, respectively. They demonstrate the different waveform sizes of the welded interfaces due to the dynamic changes in impact angle and collision velocity during the MPW process[39,40]. In addition, the waveforms at the two MPW interfaces are not sinusoidal, due to the difference in hardness of the two weld base materials. When the discharge energy is increased, the wavy structure at the Mg/Al interface appears to undergo a tangible change, transforming from a regular wave into an irregular one. The Mg/Al interfacial side contains a transition zone, mainly on the Al side. We found that a discontinuous distribution in the transition zone becomes a continuous distribution in the wavy interface area with raised discharge energy and its maximum thickness reaches 13.53μm, as indicated by white line (b)(d) in Fig. 6. The presence of hole defects in the transition zone of the Mg/Al interface has been observed as the discharge energy is 32 kJ. These defects include micron-sized holes, indicated

by blue arrows, and submicron-sized holes, indicated by white arrows in Fig. 6(c)(d). The actual mechanism of this cavitation has not been studied, but some scholars have suggested that voids are created by localized melting and solidification of the material at the interface[41,42]. It is the presence of thicker transition zones and holes that cause the low quality of their welded joints. The discharge energy has a minimal impact on the waveform of the welded interface on the Al/Fe side as shown in Fig. 6(e-h). There is a transition zone at the interface on the Al/Fe side, and it also exists on the Al-based side, as shown in the area labeled by the white line in Fig. 6(f)(h). To form the transition zone, some scholars suggest that the high-speed impact of the material causes intense plastic deformation. This results in heat accumulation at the weld interface and the creation of a high-temperature environment at the weld. Meanwhile, high pressures, high temperatures, and concentration differences promote the migration and diffusion of atoms in localized areas of the weld interface, as well as migrating and diffusing atoms in high-temperature areas leads to the formation of transition zones[43]. To establish a transition zone in the undulating valley, as depicted in Fig. 6(f)(h), some researchers posit that an energy transfer process occurs during the collision, hindered by periodically distributed wave crests. Following, at the welding interface, kinetic energy is transformed into thermal energy, leading to heat accumulation, atom migration, and diffusion in this wave, thereby forming a transition zone[44].

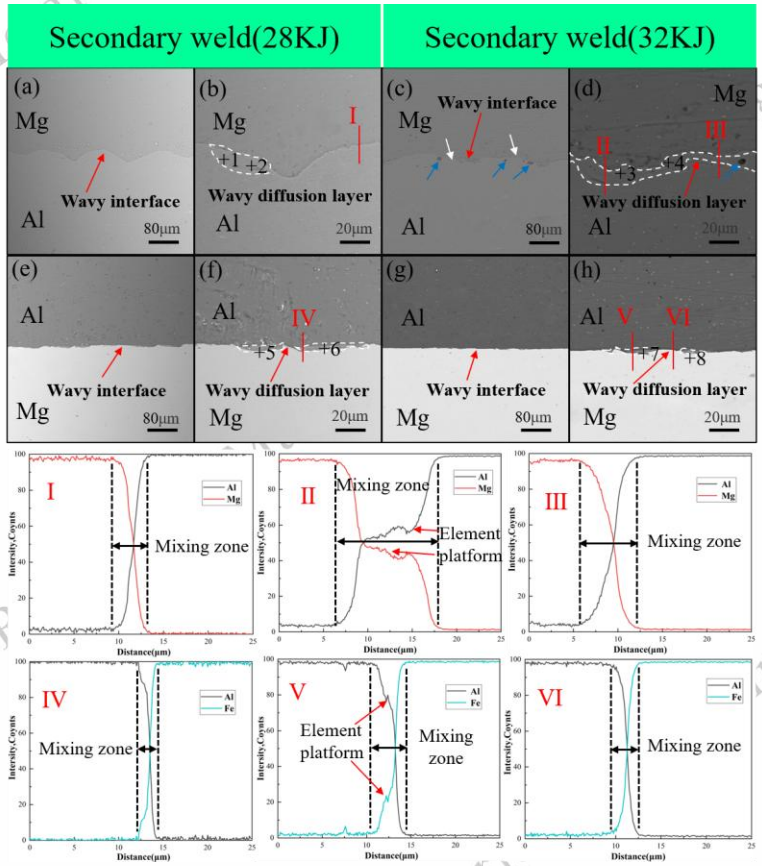

Fig. 6 SEM images and EDS line scans of Mg/Al/Fe joining interface at different discharge energies(Secondary weld): (a) (b) (e) (f) 28 KJ, (c) (d) (g) (h) 32 KJ, (a-d) for the Mg/Al side interface, (e-h) for the Al/Fe side interface.

Table 4 EDS results for points in Figures 6 and 7(atomic fraction,%).

Position	Mg	Al	Fe	Possible phase
1	51.28	48.72	-	$Al_{12}Mg_{17}$
2	59.99	40.01	-	$Al_{12}Mg_{17}$
3	40.77	59.23		Al_3Mg_2+$Al_{12}Mg_{17}$
4	45.54	54.06		Al_3Mg_2+$Al_{12}Mg_{17}$
5		87.30	12.70	$FeAl_3$+Al
6		90.85	9.15	Solid solution of Al

7	87.72	12.28	$FeAl_3$+Al
8	90.26	9.74	Solid solution of Al

To study the in-depth microstructure of the secondary welded interface, EDS line scan and point scan analyses were carried out for both Mg/Al and Al/Fe weld interfaces. As shown in Figure 6(I-VI), a certain degree of elemental diffusion is present at both welding interfaces. Due to quick high-pressure and high-temperature results in a plastic deform effect in the MPW process, different matrix metal atoms at the near interface side have to generate infiltration and convection, ultimately leading to mutual diffusion between atoms[45]. The result of line scanning in the Mg/Al interfacial side is shown in Fig. 6(I-III). The results of elemental line scanning present that the maximum diffusion width of Mg and Al elements in the reaction zone at the weld interface containing the transition zone is approximately 13.53 μm. In comparison, the maximum width of the reaction layer in the non-transition zone is approximately 3 μm. The melting and mixing of the base materials on both sides of the interface can produce extremely complex microstructure at the transition zone. The content of Mg is slightly lower than that of Al in the transition zone, and there is an approximate "plateau" between their contents in this region, as shown in Fig. 6(II). It is difficult to explain this change from the point of view of elemental diffusion science. By comparing the results of the line scans of the non-transition region, as shown in Fig. 7(I) (III), it can be surmised that this transition region produces Mg compounds. Based on the atomic composition ratios and the alloy phase diagram of Mg-Al[46], the results of the point scans in Table. 4 can be deduced that the $Al_{12}Mg_{17}$ intermetallic compounds(IMCs) were exhibited in the transition region of the Mg/Al bonding interface when the discharge energy was 28 KJ, while a mixed IMCs of Al_3Mg_2+$Al_{12}Mg_{17}$ was generated in the transition region of the Mg/Al bonding interface when the discharge energy was 32 KJ. For the Mg side tensile fracture under discharge energy at 28KJ implement XRD analysis as shown in Fig.8(f). It can be seen that the Mg phase has the strongest diffraction peak signal, while the aluminum phase is not detected, indicating that interfacial failure has occurred on the Mg side of the interface. The regions examined the $Al_{12}Mg_{17}$ phase, which conforms to the intermetallic compound generation of $Al_{12}Mg_{17}$ at the Mg/Al side interface. Interdiffusion of Al elements with Fe elements was also noted at the Al/Fe bonding interface, as shown in Fig. 6(IV-VI). Elemental line scan results show that Al and Fe elements diffuse about 4 μm in the transition zone welded interface and about 1.5 μm in the non-transition zone, with a table-like distribution in the transition zone line scan. The atomic percentages of Al and Fe are about 87% and 13%, respectively, as shown in Table 4. Based on the alloy phase diagram of Al-Fe[47], it can be deduced that there are FeAl3 intermetallic compounds in the transition zone and a solid solution of Al. The Mg/Al side interface comparing that of Al/Fe has a thicker and more transition zone, resulting in failures occurring on the Mg side. Furthermore, we discovered that the transition zone transfers discontinuous distribution into a continuous distribution existing in the interface with increasing energy, and there is a hole defect in the transition zone. This is what causes its performance to degrade at higher energies[48].

By comparing Figures 5 and 6 show that the thickness of the diffusion layer at the interface of the Secondary weld is deeper than that of the primary weld, which suggests that the Secondary weld has a fuller response at the elemental distribution level than the corresponding primary weld. This is confirmed in the EDS line sweep plots. The interface of the Primary weld is generally straight, while the Secondary weld shows a waveform, and the higher the discharge energy the more prone to shear waves. Contrast Tables 3 and 4, although the Secondary weld has a thicker diffusion layer and transition zone than the Primary weld, it also leads to the generation of more IMCs and pore defects. In the comparison of the Mg/Al and Fe/Al interfaces of Primary and Secondary welding, respectively, the evolution of the Mg/Al interface is more drastic than that of the Fe/Al interface under both discharge energies; for Primary welding, the welding energy tends to be allocated to the Mg/Al interface, whereas in the Secondary welding process, the evolution of this interface stems from the differences in the physical properties of the metal materials themselves[49,50].

2.3 Fracture morphology and failure analysis

To comprehend the joint's bonding and fracture failure mechanism, we analyzed the fracture of the samples under various discharge energies. The morphology and EDS elemental analysis of the Primary weld fracture is shown in Fig. 7, in which (a-c) are the Mg-side fracture at 32 KJ discharge

energy, and (d-f) are the Fe-side fracture at 28 KJ discharge energy. The interfaces of these two kinds of fracture are relatively flat, in which some microcracks are generated after the fracture at the Fe/Al interface; combined with Fig. 4(a)(b), it can be seen that a large number of incompletely melted particles in the transition zone of Fe/Al lead to the generation of microcracks at the fracture. In contrast, there are fewer incompletely melted particles in the transition layer of the Mg/Al interface, and thus no microcracks are detected. Analysis of the elemental distribution at the fracture revealed that the elements did not diffuse into each other, which indicated that the Primary weld interface was insufficiently bonded. In summary, the fracture of the Primary weld interface was attributed to the incompletely melted particles and the short diffusion distance of the elements; the former caused stress concentration during the tensile shear testing process, and the latter resulted in a weak metallurgical bonding between the interfaces.

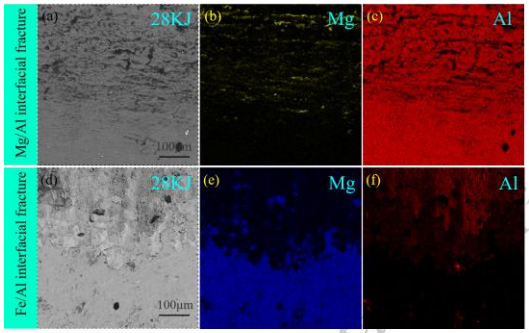

Fig. 7 Typical fracture characteristics and element distribution at Primary welded interface of MPW: (a-c) Mg-side section, (d-f) Fe-side section

Figure 8 shows the interface characteristics and EDS point scan analysis of the Secondary welded fracture at 28 KJ discharge energy. Since the fracture is concentrated on the Mg/Al side, we selected different positions of the annular weld to analyze it. A macroscopic view of the ring-binding region of the Mg side interface failure is illustrated in Figure 8a. Enlarged views of zones I and II in the Mg-side annular weld of Figure 8a are shown in Figures 8b and d. In region I, the fracture is characterized by brittle fracture, and the section is dominated by loose tissue. The EDS spectrum of this area shows the coexistence of Mg and Al and, based on previous analysis, it is known that the fracture occurred in the transition zone of the weld interface. Fractures in Region II are dominated by shear fossae of varying sizes and continuous distribution. Ultra-high velocity collision MPW creates a multitude of cavities in the ligamentous fossa region, potentially leading to the instantaneous generation of highly non-equilibrium solidified eutectic organizations[51]. According to the EDS spectroscopy analysis, the dimples are primarily composed of Mg elements, while some of the "inclusions" contain both Mg and Al elements, which may form a highly non-equilibrium solidification pseudo-eutectic structure of Mg-Al, as shown in the XRD results in Figure 8f. This shows that there is a shear stress and bending moment of the coupling effect due to this asymmetric structure in the tensile test process, in the outer side of the annular weld being prone to stress concentration, resulting in cracks firstly generated at the outer edge, and then extended to the shear dimples area, ultimately spreading to the entire annular bonding area of the inner edge until the interface failure.

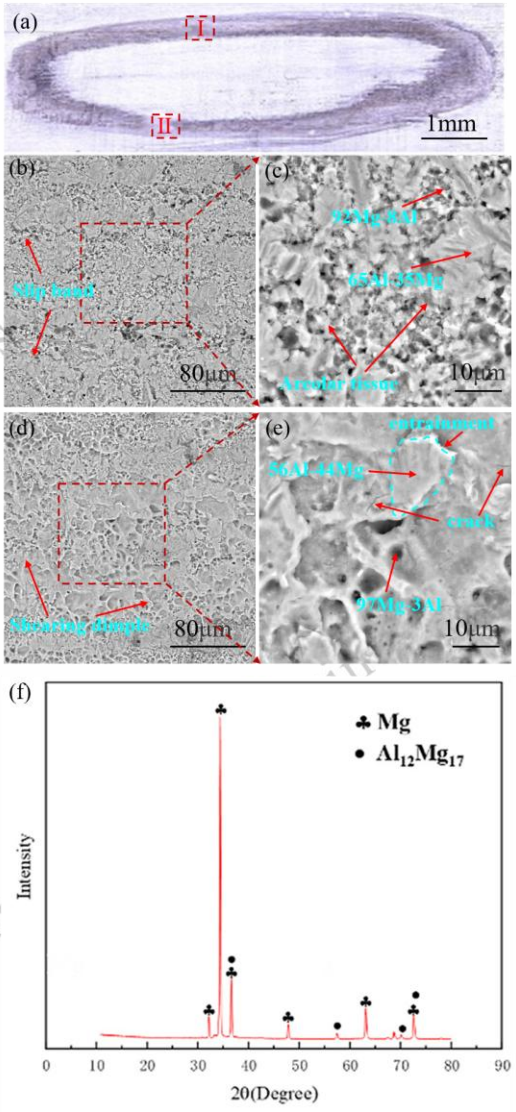

Fig. 8 Typical features of magnetic pulse welded Mg-Fe heterogeneous tensile lap shear: (a) Mg-side section, (b,d) magnified view of zones I and II, (d)(e) Figures are magnified views of b and d, (f) XRD of Mg-side section.

3 Conclusions

1) The interfacial transition zone and its morphology are mainly subjected to the discharge energy. The Primary welding interface has a straight interface and the existence of an incomplete melting layer. As the discharge energy increases, the thickness of the incompletely melted layer gradually decreases, which is caused by the random distribution of energy in the welding process. With the discharge energy increases, the Secondary weld interface is transformed from a discontinuous wave to a continuous shear wave, which also leads to the generation of micron-sized hole defects.

2) According to the bonding features at the interfacial transition zone, it can be concluded that the welded interface between the Mg/Fe dissimilar material and the Al interlayer is formed by a combination of mutual diffusion of the elements and mechanical bonding. In the MPW process, the Al interlayer acts as a bridge to achieve good weldability between Mg/Fe dissimilar materials by deformation and diffusion.

3) We noticed the existence of a transition zone in the two welding interfaces, where the transition zone at the Mg/Al side interface is composed of Al_3Mg_2 and $Al_{12}Mg_{17}$ brittle intermetallic compounds, whereas the transition zone is made up of $FeAl_3$ brittle intermetallic compounds.

Reference

1. Hovorun T P, Sumy State University, 2 Rymskogo-Korsakova St., 40007, Sumy, Ukraine, Pererva V I, et al. Modern materials for automotive industry[J]. *Journal of Engineering Sciences*, 2017, 4(2): f8-f18.
2. Jiang X, Chen S. Texture evolution and plastic deformation mechanism in magnetic pulse welding of dissimilar Al and Mg alloys[J]. *Welding in the World*, 2018, 62(6): 1159-1171.
3. Ansari N, Alabtah F G, Albakri M I, et al. Post processing of additive manufactured Mg alloys: current status, challenges, and opportunities[J]. *Journal of Magnesium and Alloys*, 2024, 12(4): 1283-1310.
4. Cheng J, Hu X, Sun X. Molecular dynamics study on interface formation and bond strength of impact-welded Mg-steel joints[J]. *Computational Materials Science*, 2020, 185: 109988.
5. Song G, Li T, Yu J, et al. A review of bonding immiscible Mg/steel dissimilar metals[J]. *Materials*, 2018, 11(12): 2515.
6. Liu L, Xiao L, Feng J, et al. Bonding of immiscible Mg and Fe via a nanoscale Fe2Al5 transition layer[J]. *Scripta Materialia*, 2011, 65(11): 982-985.
7. Kasai H, Morisada Y, Fujii H. Dissimilar FSW of immiscible materials: steel/magnesium[J]. *Materials Science and Engineering: A*, 2015, 624: 250-255.
8. Jana S, Hovanski Y, Grant G J. Friction stir lap welding of magnesium alloy to steel: a preliminary investigation[J]. *Metallurgical and Materials Transactions A*, 2010, 41(12): 3173-3182.
9. Liu L, Ren D, Liu F. A review of dissimilar welding techniques for magnesium alloys to aluminum alloys[J]. *Materials*, 2014, 7(5): 3735-3757.
10. Elthalabawy W M, Khan T I. Microstructural development of diffusion-brazed austenitic stainless steel to magnesium alloy using a nickel interlayer[J]. *Materials Characterization*, 2010, 61(7): 703-712.
11. Elthalabawy W M, Khan T I. Eutectic bonding of austenitic stainless steel 316L to magnesium alloy AZ31 using copper interlayer[J]. *The International Journal of Advanced Manufacturing Technology*, 2011, 55(1-4): 235-241.
12. Yuan X jian, Sheng G min, Luo J, et al. Microstructural characteristics of joint region during diffusion-brazing of magnesium alloy and stainless steel using pure copper interlayer[J]. *Transactions of Nonferrous Metals Society of China*, 2013, 23(3): 599-604.
13. Song G, Li T, Chen L. The mechanical properties and interface bonding mechanism of immiscible Mg/steel by laser–tungsten inert gas welding with filler wire[J]. *Materials Science and Engineering: A*, 2018, 736: 306-315.
14. Li T, Song G, Yu P, et al. Interfacial microstructure evolution in fusion welding of immiscible Mg/Fe system[J]. *Materials & Design*, 2019, 181: 107903.
15. Zhao X, Wang D, Gao J, et al. The effect of Ni foil on the interface microstructure and mechanical properties of laser lap welded steel/Mg joint[J]. *Journal of Materials Research and Technology*, 2022, 19: 4672-4682.
16. Liu L, Xiao L, Feng J C, et al. The mechanisms of resistance spot welding of magnesium to steel[J].

Metallurgical and Materials Transactions A, 2010, 41(10): 2651-2661.

17. Zhang K, Wu L, Tan C, et al. Influence of Al-Si coating on resistance spot welding of Mg to 22MnB5 boron steel[J]. *Journal of Materials Processing Technology*, 2019, 271: 23-35.
18. Patel V K, Bhole S D, Chen D L. Formation of zinc interlayer texture during dissimilar ultrasonic spot welding of magnesium and high strength low alloy steel[J]. *Materials & Design*, 2013, 45: 236-240.
19. Gong M, Lai Z, Li C, et al. Standoff-free vaporizing foil actuator welding: process principle, experimental validation, and mechanisms analysis[J]. *Journal of Manufacturing Processes*, 2024, 131: 478-493.
20. Du F, Deng L, Wang X, et al. Study on interfacial characteristics and properties of NiTi/Al–Mg joint by vaporizing foil actuator welding[J]. *Journal of Materials Research and Technology*, 2022, 20: 3429-3440.
21. Prabu S S M, Aravindan S, Ghosh S, et al. Solid-state welding of nitinol shape memory alloys: A review[J]. *Materials Today Communications*, 2023, 35: 105728.
22. Kapil A, Sharma A. Magnetic pulse welding: an efficient and environmentally friendly multi-material joining technique[J]. *Journal of Cleaner Production*, 2015, 100: 35-58.
23. Chen S J, Yu Y, Xia Y, et al. Analysis of the heat generation mechanism between the interfaces of Al-Mg magnetic pulsed welded bonds[J]. *Rare Metal Materials and Engineering*, 2013, 42(5): 998-1002.
24. Chen S J, Yu Y, Xia Y, et al. Study on interface morphology of Al-Mg alloy by magnetic pulse welding[J]. *Rare Metal Materials and Engineering*, 2012, 41(2): 352-355.
25. Zhu C C, Meng Y F, Liu Q X X, et al. Study on welding process and mechanical properties of Al/Mg dissimilar metal sheet by magnetic pulse welding[J]. *Precision Forming Engineering*, 2021, 13(4): 45-51.
26. Wang P Q, Chen D L, Ran Y, et al. Electromagnetic pulse welding of Al/Cu dissimilar materials: microstructure and tensile properties[J]. *Materials Science and Engineering: A*, 2020, 792: 139842.
27. Li J S, Sapanathan T, Raoelison R N, et al. On the complete interface development of Al/Cu magnetic pulse welding via experimental characterizations and multiphysics numerical simulations[J]. *Journal of Materials Processing Technology*, 2021, 296: 117185.
28. Sapanathan T, Raoelison R N, Buiron N, et al. In situ metallic porous structure formation due to ultra high heating and cooling rates during an electromagnetic pulse welding[J]. *Scripta Materialia*, 2017, 128: 10-13.
29. Yang Y, Luo Z, Zhang Y, et al. Dissimilar welding of aluminium to steel: a review[J]. *Journal of Manufacturing Processes*, 2024, 110: 376-397.
30. Geng H, Mao J, Zhang X, et al. Formation mechanism of transition zone and amorphous structure in magnetic pulse welded Al-Fe joint[J]. *Materials Letters*, 2019, 245: 151-154.
31. Geng H, Sun L, Li G, et al. Fatigue fracture properties of magnetic pulse welded dissimilar Al-Fe lap joints[J]. *International Journal of Fatigue*, 2019, 121: 146-154.
32. Ghosh P, Patra S, Chatterjee S, et al. Microstructural evaluation of magnetic pulse welded plain carbon steel sheets[J]. *Journal of Materials Processing Technology*, 2018, 254: 25-37.
33. Wang S, Zhou B, Zhang X, et al. Mechanical properties and interfacial microstructures of magnetic pulse welding joints with aluminum to zinc-coated steel[J]. *Materials Science and Engineering: A*, 2020, 788: 139425.
34. Yuan S C, Zhang W T, Chen Y H, et al. Effect of welding process parameters on microstructure and mechanical properties of Ti/Al dissimilar metal magnetic pulse welded joints[J]. *Electric Welding Machine*, 2022, 52(6): 118-125.
35. Xie J, Zhang W, Chen Y, et al. Interfacial microstructure and mechanical properties of the Al/Ti joint by magnetic pulse welding[J]. *Materials Characterization*, 2022, 194: 112462.
36. Huang W J. Magnetic Pulse Welding Process and Joint Properties of Al-Ti Pipe Fittings[D]. *Nanchang Hangkong University*, 2024.
37. Faes K, Kwee I, De Waele W. Electromagnetic pulse

welding of tubular products: influence of process parameters and workpiece geometry on the joint characteristics and investigation of suitable support systems for the target tube[J]. *Metals*, 2019, 9(5): 514.

38. Patra S, Arora K S, Shome M, et al. Interface characteristics and performance of magnetic pulse welded copper-steel tubes[J]. *Journal of Materials Processing Technology*, 2017, 245: 278-286.
39. Yan Y B, Zhang Z W, Shen W, et al. Microstructure and properties of magnesium AZ31B–aluminum 7075 explosively welded composite plate[J]. *Materials Science and Engineering: A*, 2010, 527(9): 2241-2245.
40. Xie J L, Peng C C, Xie W X, et al. Study on the organization and properties of magnetic pulsed welded joints of Al/Mg dissimilar alloys[J]. *Materials Reports*, 2023, 37(5): 175-179.
41. Wu X, Shang J. An investigation of magnetic pulse welding of Al/Cu and interface characterization[J]. *Journal Of Manufacturing Science And Engineering-transactions Of The ASME*, 2014, 136(5): 51002.
42. Oliveira I V, Cavaleiro A J, Taber G A, et al. Magnetic pulse welding of dissimilar materials: aluminum-copper[M]. *Materials Design and Applications: Vol. 65. Cham: Springer International Publishing*, 2017: 419-431.
43. Geng H, Xia Z, Zhang X, et al. Microstructures and mechanical properties of the welded AA5182/HC340LA joint by magnetic pulse welding[J]. *Materials Characterization*, 2018, 138: 229-237.
44. Li Y, Yang D, Yang W, et al. Effect of annealing temperature on microstructure and properties of Al/Mg magnetic pulse welding joints[J]. *Materials*, 2022, 15(16): 5519.
45. Chen S, Han Y, Gong W, et al. Mechanical properties and joining mechanism of magnetic pulse welding of aluminum and titanium[J]. *The International Journal of Advanced Manufacturing Technology*, 2022, 120(11-12): 7115-7126.
46. Niu S Y. Forming and microstructure of FSLW joints based on Mg/Al heterogeneous materials with added Zn[D]. *Shenyang Aerospace University*, 2020.
47. Atabaki M M, Nikodinovski M, Chenier P, et al. Welding of aluminum alloys to steels: an overview[J]. *Journal for Manufacturing Science and Production*, 2014, 14(2): 59-78.
48. Hu T, Pan H, Zhu P, et al. Microstructure homogeneity and its role in the mechanical properties of the magnetic pulse welded steel/Al tubular joint[J]. *Journal of Materials Research and Technology*, 2024, 30: 7076-7083.
49. Geng H H. Study on Al-Fe magnetic pulse welding and its joint failure mechanism[D]. *Hunan University*, 2021.
50. Zhu C C. Microstructure evolution and bonding mechanism at the interface of Al/Mg heterogeneous metal magnetic pulse welding[D]. *Hunan University*, 2023.
51. Wang P Q. Properties of dissimilar metal magnetic pulse welded joints and interfacial bonding mechanism[D]. *Southwest University*, 2023.

镁/钢异种金属磁脉冲焊接接头组织和性能的研究

摘要：本文采用磁脉冲焊接技术对 AZ31B 镁合金/DC56D 钢异种不相容金属进行了焊接。对比研究了一次焊和二次焊对被焊界面的影响。通过扫描电子镜(SEM)、能谱仪(EDS) 和 X 射线衍射(XRD)等分析方法对焊接接头的宏观形貌、微观组织、界面结构进行了研究。研究结果表明，铝中间层通过变形和扩散作为桥梁，实现了镁/钢异种不相容金属的磁脉冲焊接。研究发现 AZ31B/Al1060 界面呈现是典型的波形界面，在接头界面中存在过渡区，过渡层中可能生成了非常复杂的微观组织结构，其组织明显不同于两侧的 AZ31 镁合金和 1060 铝组织，可能是 Al_3Mg_2 和 $Al_{12}Mg_{17}$ 的脆性金属间化合物，过渡区主要存在铝侧，最厚处约为 13.53μm。在二次焊过渡区中发现微米级孔洞缺陷，一次焊界面出现不同厚度的不完全熔化层。Al1060/DC56D 界面主要是平直界面，在接头界面中只有少量过渡区断续分布在界面上，过渡区存在 $FeAl_3$ 脆性金属间化合物，最厚处约为 3μm。

关键词：磁脉冲焊接；力学性能；显微组织；断口形貌；一次焊和二次焊